Toward High-Performance HTL-Free All-Perovskite Tandem Solar Cells: SCAPS Simulation

Hongliang Liu, Ling Xiang, Qing Liu, Peng Gao, Yong Zhang ⓘ, Shuti Li ⓘ, and Fangliang Gao ⓘ

Abstract—**Perovskite tandem solar cells have met attractive concentrations with the potential to break through the Shockley–Queisser limit in single-junction photovoltaics. However, the efficiency of all-perovskite tandem solar cells is still challenging due to the deficiency of low-bandgap Pb–Sn mixed perovskite solar cells. In this work, high-performance hole-transporting layer free (HTL-free) low-bandgap perovskite (1.29 eV) tandem solar cells are simulated with 1-D solar cell capacitance simulator. By optimizing work function, thickness, and doping concentration of the perovskite layer, the power conversion efficiency (PCE) of HTL-free perovskite device reached to 19.14%. Furthermore, the all-perovskite tandem solar cell combined this HTL-free solar cell with $MAGeI_3$ (1.9 eV) top solar is studied and the current matching condition between two subcells is obtained by the optimum thicknesses of perovskite layers, which are 700 and 350 nm for the bottom and top absorbers, respectively. The all-perovskite tandem solar cell reaches a PCE of 29.1%, which is among one of the top efficiency in perovskite-based solar cells.**

Index Terms—**1-D solar cell capacitance simulator (SCAPS-1D), all-perovskite tandem solar cells, hole-transporting layer free (HTL-free) perovskite solar cells (PSCs).**

I. INTRODUCTION

IN THE past decade, researchers have met the rapid development of solution-processed perovskite solar cells (PSCs) with long carrier diffusion length [1], tunable bandgap [2], and flexible potential [3]. However, due to thermal and nonradiative recombination loss, the power conversion efficiency (PCE) of single-junction has been limited to 33% [4]. A promising strategy of breaking through the limitation is to multiple the light harvesting absorber to develop tandem solar cells. Accordingly,

Hongliang Liu, Ling Xiang, Qing Liu, Yong Zhang, Shuti Li, and Fangliang Gao are with the Guangdong Engineering Research Center of Optoelectronic Functional Materials and Devices, School of Semiconductor Science and Technology, Institute of Semiconductors, South China Normal University, Foshan 528225, China (e-mail: lhlmax@foxmail.com; 17857098021@163.com; qingliu6823@163.com; zycq@scnu.edu.cn; lishuti@scnu.edu.cn; gaofl@m.scnu.edu.cn).

Peng Gao is with the Tianjin Institute of Power Sources, Tianjin 300384, China (e-mail: gplvff@sina.com).

many efforts have been done to combine PSCs with silicon [5], copper indium gallium selenide (CIGS) [6], and GaAs [7]. However, the rigid formation condition of these materials is not desirable for low-cost solution-procession [8]. In this regard, combining low-bandgap with wide-bandgap perovskite, along with the all-solution-processed superiority, provides a novel structure of monolithic tandem solar cells, which offer the potential of high efficiency to exceed the limit of single-junction PCS [9].

Recently, Sn containing perovskite film (E_g < 1.3 eV) with low-toxic, suitable bandgap, and wide light-harvesting range becomes a hot topic for its further environmentally friendly application [10], [11], [12], [13], [14], [15]. However, this low-bandgap PSCs suffer from poor performance due to instability and poor reproducibility caused by self-oxidation of Sn^{2+} to Sn^{4+}, which hampers the application of PSCs. As a result, the poor performance and stability of low-bandgap PSCs hinders the overall development of all-perovskite tandem solar cells.

Besides, recent work shows that the PSC without cost-effective hole-transporting layer (HTL) can deliver enhanced stability and comparable performance with their HTL-containing counterparts via energy level alignment and molecular doping. For example, Tsai et al. [16] reported that MA cation in $MAPbI_3$ film could interact with the unprotonated oxygen on the surface of indium tin oxide (ITO) via hydrogen bonding, which increased the work function from 4.7 to 5.0 eV. With better energy alignment with $MAPbI_3$, the HTL-free devices delivered the best efficiency over 11%. Wu et al. [12] introduced F_4TCNQ small molecular into PSCs to reduce the series resistance of the devices. With doping the small molecular, carrier concentration has increased four times (0.6×10^{16} cm^{-3} for neat $MAPbI_3$ and 2.4×10^{16} cm^{-3} for added with F_4TCNQ). This doping strategy could be favorable for the formation of HTL-free p-n heterojunction by increasing the work function of perovskite, which could eventually result in an upward band bending at the ITO/perovskite interface with facilitated hole transfer. Moreover, McMeekin et al. [17] developed a facile way to introduce cooper into perovskite film, thus manipulating Fermi level approaching ITO. Enhanced charge separation and collection would contribute to better energy level alignment, leading to a high PCE of 15.84% with inverted HTL-free PSCs. Recently, Prasanna et al. [14] found that translating HTL-free $FA_{0.75}Cs_{0.25}Sn_{0.4}Pb_{0.6}I_3$ (1.29 eV) PSCs into the all-perovskite tandem application makes it comparable with the HTL-containing counterpart. This work put new insight into a simple and cost-effective all-perovskite tandem solar cell configuration with a novel structure.

TABLE I
MATERIAL PARAMETER USED IN THE SIMULATION

	PEDOT:PSS	FA$_{0.75}$Cs$_{0.25}$Sn$_{0.4}$Pb$_{0.6}$I$_3$	C$_{60}$	MAGeI$_3$	CuI
E_g (eV)	1.8	1.29	1.7	1.9	3.1
X (eV)	3.5	3.6	4.5	3.98	2.1
$\varepsilon/\varepsilon_0$	10	9.93	10	10	6.5
N_c (cm^{-3})	2.2×10^{18}	1×10^{19}	2.2×10^{18}	1×10^{16}	2.8×10^{19}
N_v (cm^{-3})	1.8×10^{19}	1×10^{18}	1.8×10^{19}	1×10^{15}	1×10^{19}
μ_e (cm^2/Vs)	2×10^{-2}	1.5×10^3	2	1.62×10^2	1×10^2
μ_h (cm^2/Vs)	8×10^{-1}	5.85×10^2	2	1.01×10^2	4.39×10^1
N_D (cm^{-3})	-	-	1×10^{13}	1×10^9	-
N_A (cm^{-3})	1×10^{16}	1×10^{15}	1×10^{17}	1×10^9	1×10^{18}

In this work, we have systematically carried out a simulation of HTL-free low-bandgap PSCs and their tandem application. 1-D solar cell capacitance simulator (SCAPS-1D) software developed by Burgelman et al. [18] is utilized to explore HTL-free devices and tandem solar cells. The HTL-free low-bandgap PSC shows a high PCE of 19.1%. When further combined low-bandgap absorber with wide-bandgap MAGeI$_3$ top absorber, a champion PCE of 29.1% can be achieved.

II. EXPERIMENTAL SECTION

SCAPS-1D is a 1-D optoelectrical simulator that provides an approach to simulate the basic parameters of absorbing layers and transportation layers with the number of layers up to seven at most. It is widely applied in investigating crystalline solar cells to further predict the device performance with device structure, bulk/interface defect, as well as operation condition. The software is fundamentally based on Poisson's (1), hole continuity (2), and electron continuity (3)

$$\frac{d}{dx}\left(-\varepsilon(x)\frac{d\psi}{dx}\right)$$
$$= q\left[p(x)-n(x)+N_d^+(x)-N_a^-(x)+p_t(x)-n_t(x)\right] \tag{1}$$

$$\frac{dp_n}{dt} = G_p - \frac{p_n - p_{n0}}{\tau_p} - p_n\mu_p\frac{d\xi}{dx} - \mu_p\xi\frac{dp_n}{dx} + D_p\frac{d^2p_n}{dx^2} \tag{2}$$

$$\frac{dn_p}{dt} = G_n - \frac{n_p - n_{p0}}{\tau_n} + n_p\mu_n\frac{d\xi}{dx} + \mu_n\xi\frac{dn_p}{dx} + D_n\frac{d^2n_p}{dx^2} \tag{3}$$

where ε is dielectric constant, ψ the electrostatic potential, q is the electron charge, D is diffusion coefficient, ξ is permittivity, n, p, n_t, and p_t are the densities of free electrons, free holes, trapped electrons, and trapped holes, respectively, N_a^- refers to ionized acceptor-like doping concentration, and N_d^+ for ionized donors, such as doping concentration.

To illustrate the topic of HTL-free low bandgap PSCs, we first simulate HTL-containing PSCs. As shown in Fig. 1, the device structure is composed of ITO/PEDOT:PSS/FA$_{0.75}$Cs$_{0.25}$Sn$_{0.4}$Pb$_{0.6}$I$_3$/C$_{60}$/metal contact. For HTL-free devices, PEDOT:PSS HTL is removed to construct HTL-free devices as ITO/FA$_{0.75}$Cs$_{0.25}$Sn$_{0.4}$Pb$_{0.6}$I$_3$/C$_{60}$/metal contact. The basic parameters of each layer are derived according
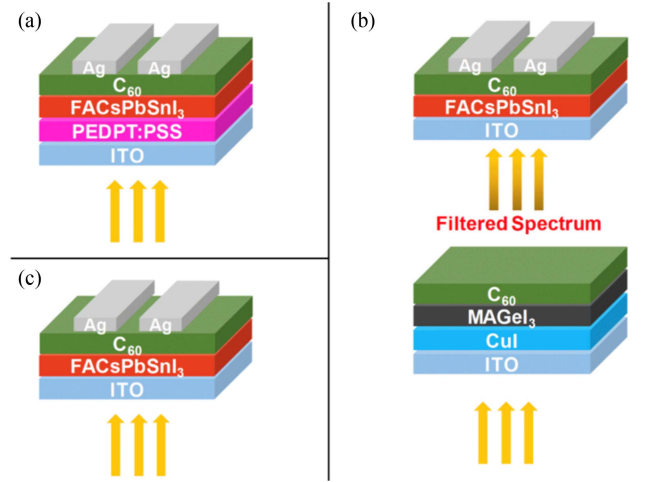

Fig. 1. Device structure of (a) HTL-containing solar cell, (b) HTL-free solar cell, and (c) tandem solar cell.

to previous reports and are summarized in Table I [14], [19], [20], [21]. The distribution of defects in perovskite films is according to previous work by Duan et al. [22] using Gauss and beta-function distribution. As illustrated in Fig. 1(c), MAGeI$_3$ top cells are first calibrated under standard AM 1.5G spectrum [19], [20]. To combine two standalone absorbers, the absorption spectrum of the top cell is performed by (4). Transmitted spectrum is further obtained by filtering AM 1.5G spectrum with the absorption of each layer in the top cell via (5). In this case, the filtered spectrum is adopted as the input incident spectrum of low-band perovskite bottom cell subsequently. This situation may be owing to the limitations of SCAPS-1D software, and ideal tunnel junction between the top and bottom cell is assumed without recombination loss. At last, the top cell and filtered bottom cell are combined with a current matching technique to approach the parameters of final two-terminal tandem solar cells. This method for approaching tandem parameters will be further discussed in detail later

$$\alpha(\lambda) = A\sqrt{hv - E_g} \tag{4}$$

$$S(\lambda) = S_0(\lambda) * \exp\{-(\alpha_{CuI} * d_{CuI}$$
$$+ \alpha_{MAGeI_3} * d_{MAGeI_3} + \alpha_{C_{60}} * d_{C_{60}})\} \tag{5}$$
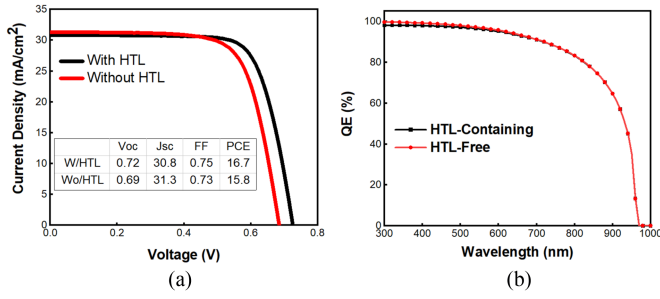
Fig. 2. (a) I–V curves and (b) EQE curves for HTL-containing and HTL-free devices.

where α and E_g are the absorption and bandgap of each layer, respectively. $S_0(\lambda)$ is the standard AM1.5G spectrum, and d is the thickness of each layer.

All the simulation is conducted at working temperature of 300 K with a series resistance of 1 Ω. Fundamental optical model equations used in this study follow (6)–(8)

$$N_{phot}(\lambda, x)$$
$$= N_{phot0}(\lambda, x) * T_{front}(\lambda) * \exp(-x * \alpha(\lambda))$$
$$* \left[\frac{1 + R_{back}(\lambda) * \exp(-2(d-x)\alpha(\lambda))}{1 - R_{back}(\lambda) * R_{int} * \exp(-2d * \alpha(\lambda))} \right] \quad (6)$$

$$G(\lambda, x) = \alpha(\lambda, x) * N_{phot}(\lambda, x) \quad (7)$$

$$G(x) = \int_{\lambda_{min}}^{\lambda_{max}} G(\lambda, x) \, d\lambda$$
$$= \int_{\lambda_{min}}^{\lambda_{max}} \alpha(\lambda, x) * N_{phot}(\lambda, x) \, d\lambda \quad (8)$$

where N_{phot} is the photon flux at each position of layers, N_{phot0} is the light incident photon flux, T_{front} is the transmission of the front contact, R_{back} is the reflection at the back contact, R_{int} is an internal reflection at the front contact, d is the layer thickness, x is the position in the layer, and $G(x)$ is the generation rate of electron-hole pairs. It is noteworthy that this model contains only reflection/transmission at the two contacts and absorption in the semiconductor layers. Thus, there are no interference, no scattering, and no intermediate reflectors.

III. RESULTS AND DISCUSSION

A. Simulation of HTL-Free Low Bandgap PSCs

Fig. 2(a) performs the current density–voltage for both HTL-containing and HTL-free device. The HTL-containing PSC shows PCE of 16.7% with a Voc of 0.72 V, a Jsc of 30.8 mA/cm², and FF of 0.75, in agreement with the previously reported experimental results, whereas HTL-free PSC demonstrates PCE of 15.4% with a Voc of 0.69 V, a Jsc of 31.3 mA/cm², and FF of 0.72, slightly lower than that of reported [14]. Besides, Fig. 2(b) shows the external quantum efficiency of both simulated devices. Enhanced absorption from 300 to 600 nm of HTL-free device may contribute to slightly improved Jsc. Details for simulation results are summarized in Table II.
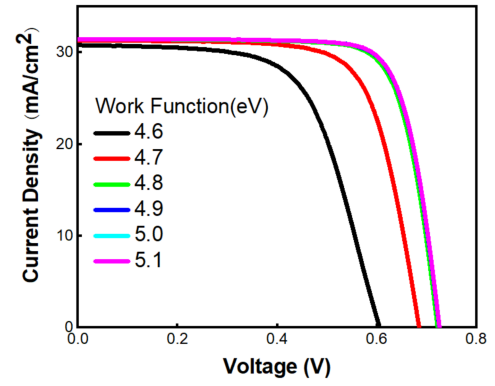

Fig. 3. I–V curves for HTL-free devices with work function varied from 4.6 to 5.1 eV.
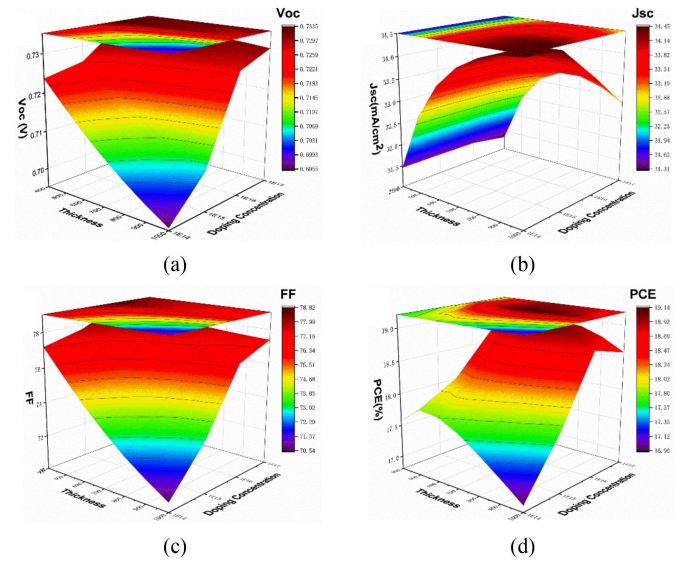

Fig. 4. 3-D contour plot of PV parameters for the low-bandgap cell: (a) Voc (b) Jsc (c) FF, and (d) PCE.

TABLE II
PV PARAMETERS OF DEVICE WITH/WITHOUT HTL

Device		Voc (V)	Jsc (mA/cm²)	FF	PCE (%)
W/HTL	Simulation	0.72	30.8	0.75	16.7
Wo/HTL	Simulation	0.69	31.3	0.72	15.4

As for HTL-free PSCs, the perovskite layer is directly contacted with metal or ITO [23]. The energy level alignment induced the shift of contact work function. It is critical for the performance since a mismatch of energy level could lead to severe interface recombination [24]. Besides, in HTL-free devices, recombination tends to take place at the interface of electrode and perovskite. Carriers motivated by the built-in electric field will separate and migrate from the perovskite layer. Sufficient driving force deduced by the built-in electric field could promote carrier separation as well as reduction of inner recombination [25]. Previous work demonstrates that contact
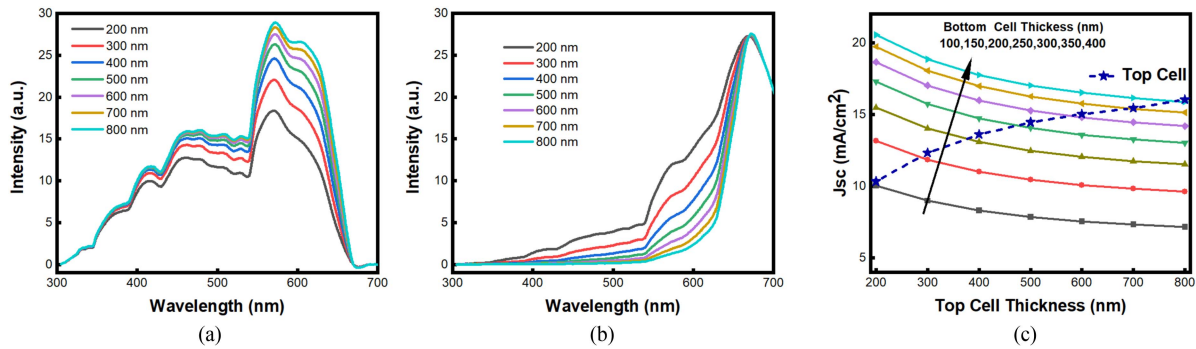
Fig. 5.   (a) and (b) Absorption and transmitted spectrum with different top cell thickness. (c) Jsc distribution for the current matching condition.

work function can be changed with surface modification, such as ion liquid [26] and organic monomolecular [27]. In this case, device performance caused by work function was firstly investigated. As depicted in Fig. 3, with the work function varies from 4.6 to 5.1 eV, the PCE of HTL-free devices increased from 11.8% to 17.8%. It may be attributed to the reinforced built-in electric field caused by increasing work function. It is noteworthy that when the work function has shifted up to 4.8 eV, the improvement of PCE becomes negligible, which may be concluded to the sufficient built-in electric field for charge extraction and migration.

One critical issue for Sn-based perovskite devices is that they always suffer from severe self n-doping due to oxidation from Sn^{2+} to Sn^{4+}, which is suspected to increase conductivity. Obviously, the formation of unwanted insulate tin oxide would like to decrease the long-range conductance. It is widely reported that doping is an effective method and widely used in PSCs [28]. However, heavy self-oxidation in Sn-based PSCs would like to cause fast recombination that tends to hinder carrier diffusion. The optimized doping concentration should be further investigated. Moreover, another key factor for device performance is the thickness of the perovskite film [29]. It is critical for carriers to move across perovskite layer reaching contact within diffusion length, whereas thicker perovskite film tends to generate more carriers, which is beneficial for device performance. In this stage, the impact of varied doping concentration and thickness is simultaneously studied.

Basic parameters of Voc, Jsc, FF, and PCE varied by doping concentration and thickness are shown in Fig. 4(a)–(d). It is notably that thickness of perovskite film plays a critical role in photovoltaic devices. By increasing the thickness of perovskite film from 400 to 1000 nm, both Voc and FF decrease continuously but Jsc increases. On the one hand, thick perovskite film will tend to generate more photos, as well as sufficient charge extraction and segregation. On the other hand, the thick perovskite film would lead to inner carrier recombination, where electrons and holes may not be able to migrate to ETL and contact [28]. Moreover, results show that Voc and FF would increase with the improvement of doping concentration, which is opposite to the tendency of slightly decreased Jsc. Finally, the champion device with a thickness of 700 nm and a doping concentration of 10^{16} provides a PCE of 19.1%, which is superior to work-function-optimized devices.

TABLE III
PV PARAMETERS OF THE TOP CELL, BOTTOM CELL, AND TANDEM CELL

Cell	Voc (V)	Jsc (mA/cm^2)	FF	PCE (%)
Top Cell	1.70	15.5	0.64	16.8
Bottom Cell	0.68	15.4	0.72	12.3
Tandem Cell	2.39	15.5	0.79	29.1

B. Simulation of All-Perovskite Tandem Solar Cells

This section dedicates to discuss the comprehensive simulation of all-perovskite tandem solar cells constructed by HTL-free low-bandgap perovskite bottom absorber and $MAGeI_3$ top absorber. The basic parameters of $MAGeI_3$ top cell (constructed with $CuI/MAGeI_3/C_{60}$) are following previous reports [19], [20].

The absorption spectra of top configuration with varied $MAGeI_3$ thickness are initially simulated utilizing the absorption parameters. The thicknesses of the top absorber are increasing from 200 to 800 nm, which are shown in Fig. 5(a). With increasing the thickness of MAGeI3, the absorption will be enhanced in the region from 300 to 700 nm. As shown in Fig. 5(b), the top cells are filtered with AM 1.5G spectrum to obtain the transmitted spectrum. The transmission intensity of the top cell significantly decreases below 700 nm wavelength with the increment of top absorber thickness. Cutoff absorption at 650 nm is in agreement with the absorption region of $MAGeI_3$.

In a two-terminal tandem solar cell, the current would travel pass through the whole device. It is crucial for both standalone devices to reach the same Jsc according to the current matching technique, where it is widely used in the tandem configuration in SCAPS-1D simulation [30]. First, the top cell with varied absorber thickness is illuminated with AM 1.5G spectrum, where filtered top cell spectra are obtained. Then different thicknesses of the bottom cell absorber are adopted under each filtered top cell spectra. In order to obtain the current matching configuration, Jsc from bottom cell filtered in different top absorber thickness are summarized in Fig. 5(c). The optimized current matching condition can be achieved with thickness under top cell (700 nm) and bottom cell (350 nm), which is desirable for further flexible application. As a result, the top cell and bottom

TABLE IV
SUMMARY OF ALL-PEROVSKITE TANDEM SOLAR CELLS

| Year	Bottom	Top	Voc (V)	Jsc (mA/cm^2)	FF	PCE (%)	Ref
2016	$FA_{0.75}Cs_{0.25}Sn_{0.5}Pb_{0.5}I_3$	$FA_{0.83}Cs_{0.17}Pb(I_{0.5}Br_{0.5})_3$	1.66	14.5	0.70	17.0	[31]
2016	$MAPbI_3$	$MAPbBr_3$	1.95	8.4	0.66	10.8	[32]
2016	$MAPbI_3$	$MAPbI_3$	1.89	6.6	0.56	7.0	[33]
2017	$MAPbI_3$	$Cs_{0.15}FA_{0.85}Pb(I_{0.3}Br_{0.7})_3$	2.29	9.8	0.80	18.1	[34]
2017	$MAPb_{0.5}Sn_{0.5}I_3$	$MAPb(I_{0.6}Br_{0.4})_3$	1.98	12.7	0.73	18.5	[35]
2018	$MAPbI_3$	$MAPbI_3$	2.30	9.8	0.79	18.0	[36]
2018	$FA_{0.75}Cs_{0.25}Sn_{0.5}Pb_{0.5}I_3$	$FA_{0.6}Cs_{0.4}Pb(Br_{0.3}I_{0.7})_3$	1.81	14.8	0.71	19.1	[29]
2018	$(FASnI_3)_{0.6}(MAPbI_{3-3x}Cl_{3x})_{0.4}:Cl$	$FA_{0.8}Cs_{0.2}Pb(I_{0.7}Br_{0.3})_3$	1.92	14.0	0.78	21.0	[8]
2019	$MASn_{0.25}Pb_{0.75}I_3$	$MAPbI_3$	1.79	13.3	0.78	18.6	[10]
2019	$FA_{0.7}MA_{0.3}Pb_{0.5}Sn_{0.5}I_3$	$FA_{0.8}Cs_{0.2}Pb(I_{0.6}Br_{0.4})_3$	1.96	15.6	0.81	24.8	[28]
2019	$FA_{0.75}Cs_{0.25}Sn_{0.5}Pb_{0.5}I_3$	$FA_{0.6}Cs_{0.3}DMA_{0.1}PbI_{2.4}Br_{0.6}$	1.88	16.0	0.77	23.1	[3]
2019	$(FASnI_3)_{0.6}(MAPbI_3)_{0.4}:GuaSCN$	$Cs_{0.5}FA_{0.8}MA_{0.15}PbI_{2.55}Br_{0.45}$	1.94	15.0	0.80	23.4	[9]
2019	$FA_{0.5}MA_{0.45}Cs_{0.05}Pb_{0.5}Sn_{0.5}I_3$	$FA_{0.6}Cs_{0.4}Pb(I_{0.65}Br_{0.35})_3$	1.99	15.1	0.77	23.0	[37]
2020	$FA_{0.75}Cs_{0.25}Sn_{0.4}Pb_{0.6}I_3$	$MAGeI_3$	2.39	15.5	0.79	29.1	This work
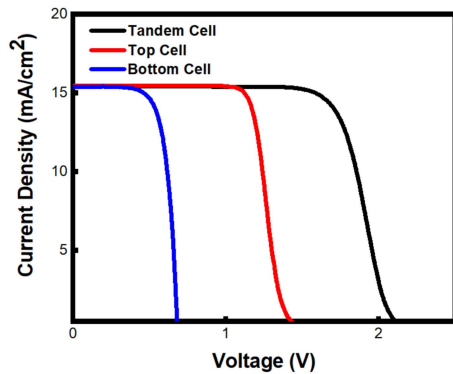
Fig. 6. *I–V* curves for the top, bottom, and tandem solar cells.

cell exhibit the same Jsc value of 15.5 mA/cm^2. The details of the photovoltaic parameters of the top cell, bottom cell, and tandem cell are shown in Table III.

Furthermore, as for the parameters of the tandem cell, Voc of both cells are summed at equal current density conditions. The tandem solar cell demonstrated PCE of 29.1% with Voc of 2.39 V, Jsc of 15.5 mA/cm^{-2}, and FF of 0.79, which is one of the most efficient all-perovskite tandem solar cells, as shown in Fig. 6. To have a better conception in this all-perovskite tandem solar cell, the recent development of this all-perovskite tandem solar cell field has been summarized in Table IV. It would be demonstrated that such all-perovskite tandem solar cells would be the next topic toward high-efficiency and cost-effective photovoltaics.

IV. CONCLUSION

In this work, a simulation of low-bandgap PSC and its tandem application has been done showing the impact of underlying parameters for further development of such HTL-free low-bandgap photovoltaics. By optimizing the work-function of the top contact, thickness, and doping concentration of perovskite film, the HTL-free low-bandgap PSC demonstrates a cheerful PCE of 19.1%. Furthermore, by coupling with $MAGeI_3$ top cell to construct all-perovskite tandem solar cells, results show that the tandem device delivers Voc of 2.39 V and PCE of 29.1%, which is one of the state-of-the-art all-perovskite tandem solar cells up to date. This work paves a new insight towards the fabrication of high-efficient and cost-effective novel structural photovoltaics.

REFERENCES

[1] Q. Dong et al., "Electron-hole diffusion lengths >175 μm in solution-grown $CH_3NH_3PbI_3$ single crystals," *Science*, vol. 347, pp. 967–970, 2015.

[2] W. S. Yang et al., "Iodide management in formamidinium-lead-halide-based perovskite layers for efficient solar cells," *Science*, vol. 356, pp. 1376–1379, 2017.

[3] A. F. Palmstrom et al., "Enabling flexible all-perovskite tandem solar cells," *Joule*, vol. 3, pp. 2193–2204, 2019.

[4] J. Madan, R. Pandey, and R. Sharma, "Device simulation of 17.3% efficient lead-free all-perovskite tandem solar cell," *Sol. Energy*, vol. 197, pp. 212–221, 2020.

[5] F. Sahli et al., "Fully textured monolithic perovskite/silicon tandem solar cells with 25.2% power conversion efficiency," *Nature Mater.*, vol. 17, pp. 820–826, 2018.

[6] M. Jošt et al., "21.6%-efficient monolithic perovskite/Cu(In,Ga)Se$_2$ tandem solar cells with thin conformal hole transport layers for integration on rough bottom cell surfaces," *Amer. Chem. Soc. Energy Lett.*, vol. 4, pp. 583–590, 2019.

[7] Z. Li et al., "Wide-bandgap perovskite/gallium arsenide tandem solar cells," *Adv. Energy Mater.*, vol. 10, 2019, Art. no. 193085.

[8] D. Zhao et al., "Efficient two-terminal all-perovskite tandem solar cells enabled by high-quality low-bandgap absorber layers," *Nature Energy*, vol. 3, pp. 1093–1100, 2018.

[9] J. Tong et al., "Carrier lifetimes of >1 μs in Sn-Pb perovskites enable efficient all-perovskite tandem solar cells," *Science*, vol. 364, pp. 475–479, 2019.

[10] C.-Y. Chang, B.-C. Tsai, Y.-C. Hsiao, M.-Z. Lin, and H.-F. Meng, "Solution-processed conductive interconnecting layer for highly-efficient and long-term stable monolithic perovskite tandem solar cells," *Nano Energy*, vol. 55, pp. 354–367, 2019.

[11] Y. Yao et al., "Highly efficient Sn-Pb perovskite solar cell and high-performance all-perovskite four-terminal tandem solar cell," *Sol. RRL*, vol. 4, 2019, Art. no. 1900396.

[12] W. Q. Wu et al., "Molecular doping enabled scalable blading of efficient hole-transport-layer-free perovskite solar cells," *Nature Commun.*, vol. 9, 2018, Art. no. 1625.

[13] I. Zimmermann, S. Aghazada, and M. K. Nazeeruddin, "Lead and HTM free stable two-dimensional tin perovskites with suitable band gap for solar cell applications," *Angewandte Chemie*, vol. 58, pp. 1072–1076, 2019.

[14] R. Prasanna et al., "Design of low bandgap tin-lead halide perovskite solar cells to achieve thermal, atmospheric and operational stability," *Nature Energy*, vol. 4, pp. 939–947, 2019.

[15] K. Lu et al., "Fermi level alignment by copper doping for efficient ITO/perovskite junction solar cells," *J. Mater. Chem. A*, vol. 5, pp. 25211–25219, 2017.

[16] K.-W. Tsai, C.-C. Chueh, S. T. Williams, T.-C. Wen, and A. K. Y. Jen, "High-performance hole-transporting layer-free conventional perovskite/fullerene heterojunction thin-film solar cells," *J. Mater. Chem. A*, vol. 3, pp. 9128–9132, 2015.

[17] D. P. McMeekin et al., "Solution-processed all-perovskite multi-junction solar cells," *Joule*, vol. 3, pp. 387–401, 2019.

[18] M. Burgelman, P. Nollet, and S. Degrave, "Modelling polycrystalline semiconductor solar cells," *Thin Solid Films*, vol. 361, pp. 527–532, 2000.

[19] A.-A. Kanoun, M. B. Kanoun, A. E. Merad, and S. Goumri-Said, "Toward development of high-performance perovskite solar cells based on $CH_3NH_3GeI_3$ using computational approach," *Sol. Energy*, vol. 182, pp. 237–244, 2019.

[20] S. Abdelaziz, A. Zekry, A. Shaker, and M. Abouelatta, "Investigating the performance of formamidinium tin-based perovskite solar cell by SCAPS device simulation," *Opt. Mater.*, vol. 101, 2020, Art. no. 109738.

[21] N. Lakhdar and A. Hima, "Electron transport material effect on performance of perovskite solar cells based on $CH_3NH_3GeI_3$," *Opt. Mater.*, vol. 99, 2020, Art. no. 109517.

[22] Q. Duan et al., "Design of hole-transport-material free $CH_3NH_3PbI_3$/$CsSnI_3$ all-perovskite heterojunction efficient solar cells by device simulation," *Sol. Energy*, vol. 201, pp. 555–560, 2020.

[23] Z. Ni et al., "Resolving spatial and energetic distributions of trap states in metal halide perovskite solar cells," *Science*, vol. 367, pp. 1352–1358, 2020.

[24] J. Madan et al., "Device simulation of 17.3% efficient lead-free all-perovskite tandem solar cell," *Optik*, vol. 202, 2020, Art. no. 163646.

[25] W. T. Wang et al., "Synergistic reinforcement of built-in electric fields for highly efficient and stable perovskite photovoltaics," *Adv. Funct. Mater.*, vol. 30, 2020, Art. no. 1909755.

[26] S. Ghosh and T. Singh, "Role of ionic liquids in organic-inorganic metal halide perovskite solar cells efficiency and stability," *Nano Energy*, vol. 63, 2019, Art. no. 103828.

[27] W. Kong et al., "Organic monomolecular layers enable energy-level matching for efficient hole transporting layer free inverted perovskite solar cells," *Amer. Chem. Soc. Nano*, vol. 13, pp. 1625–2634, 2019.

[28] R. Lin et al., "Monolithic all-perovskite tandem solar cells with 24.8% efficiency exploiting comproportionation to suppress Sn(II) oxidation in precursor ink," *Nature Energy*, vol. 4, pp. 864–873, 2019.

[29] T. Leijtens et al., "Tin-lead halide perovskites with improved thermal and air stability for efficient all-perovskite tandem solar cells," *Sustain. Energy Fuels*, vol. 2, pp. 2450–2459, 2018.

[30] G. K. Gupta and A. Dixit, "Theoretical studies of single and tandem $Cu_2ZnSn(S/Se)_4$ junction solar cells for enhanced efficiency," *Opt. Mater.*, vol. 82, pp. 11–20, 2018.

[31] G. E. Eperon et al., "Perovskite-perovskite tandem photovoltaics with optimized band gaps," *Science*, vol. 354, pp. 861–865, 2016.

[32] J. H. Heo and S. H. Im, "$CH_3NH_3PbBr_3$-$CH_3NH_3PbI_3$ perovskite-perovskite tandem solar cells with exceeding 2.2 V open circuit voltage," *Adv. Mater.*, vol. 28, pp. 5121–5125, 2016.

[33] F. Jiang et al., "A two-terminal perovskite/perovskite tandem solar cell," *J. Mater. Chem. A*, vol. 4, pp. 1208–1213, 2016.

[34] D. Forgács et al., "Efficient monolithic perovskite/perovskite tandem solar cells," *Adv. Energy Mater.*, vol. 7, 2017, Art. no. 1602121.

[35] A. Rajagopal et al., "Highly efficient perovskite-perovskite tandem solar cells reaching 80% of the theoretical limit in photovoltage," *Adv. Mater.*, vol. 29, 2017, Art. no. 1702104.

[36] J. Ávila et al., "High voltage vacuum-deposited $CH_3NH_3PbI_3$–$CH_3NH_3PbI_3$ tandem solar cells," *Energy Environ. Sci.*, vol. 11, pp. 3292–3297, 2018.

[37] Z. Yang et al., "Enhancing electron diffusion length in narrow-bandgap perovskites for efficient monolithic perovskite tandem solar cells," *Nature Commun.*, vol. 10, 2019, Art. no. 4498.